Neural networks and their applications in lithostratigraphic interpretation of seismic data for reservoir characterization

V. Singh, Repsol-YPF, Madrid, Spain
A. K. Srivastava and D. N. Tiwary, Oil and Natural Gas Corporation, Dehradun, India
P. K. Painuly, Reliance Industries Limited, Mumbai, India
Mahesh Chandra, Dehradun, India

Downloaded 12/28/14 to 129.105.215.146. Redistribution subject to SEG license or copyright; see Terms of Use at http://library.seg.org/

Modern 3D seismic data and the associated extracted attributes have allowed better description of reservoir heterogeneities and more realistic assessment of hydrocarbons in place. However, the establishment of a complicated nonlinear relationship between seismic attributes and reservoir properties has been a major challenge for working geoscientists. Recently, supervised neural networks have been used for predicting reservoir properties away from the boreholes in interwell regions after establishing the relationship between seismic attributes and well-log data. The effectiveness of these neural network techniques in 3D seismic interpretation is demonstrated in this paper through a real data example from India's Cambay Basin.

Geologic background. The prolific Cambay Basin, in the western part of the Indian subcontinent, forms the northern extension of the large Bombay offshore basin. It has attained a mature stage of hydrocarbon exploitation after nearly five decades of extensive exploration. Since the first discovery of oil in 1958, nearly 4000 wells have been drilled, resulting in the discovery of about 90 oil and gas fields with estimated most likely in-place reserves on the order of 3000 MMT of oil and oil equivalent. This basin came into existence during the Late Mesozoic with the development of major tensional faults along pre-existing basement trends following widespread extrusion of Deccan Trap basalt. This basaltic basement underlies thick Tertiary-Quaternary sediments. Based on the recognized basement fault trends, the basin has been divided into a number of blocks; the Sanchor-Patan, Mehsana-Ahmedabad, Tarapur, Broach-Jambusar, and Narmada (Figure 1). These blocks have NW–SE horst and graben features.

The study area lies in the upper part of the NW–SE Nardipur syncline in the Mehsana-Ahmedabad block of the North Cambay Basin. The Nardipur syncline is bounded by the main Kalol Field in the west, Wadu-Paliyad Field in the north, Limbodra Field in the east, and Wavel-Indrora Field in the south (Figure 2). The generalized stratigraphy of the study area is shown in Figure 3. Several prior studies have documented the existence of the essential elements of the petroleum system, namely source rock, reservoir rock, seal, and overburden, as well as the processes involved such as trap formation, generation, migration, and accumulation of hydrocarbons.

The potential source rocks in the study area are the Tarapur, Kalol, and Cambay shales. Total organic content (TOC) is 0.58–5.98% in Tarapur, 0.55–62.8% in Kalol, and 0.61–14.3% in Cambay shales. The high TOC value in Kalol is caused by the presence of coal. The vitrinite reflectance (%VR_o) and T_{max} obtained from rock evaluation pyrolysis are the most popular methods of determining the generation threshold (oil-generation window). The amount and type of organic matter and its level of thermal maturation

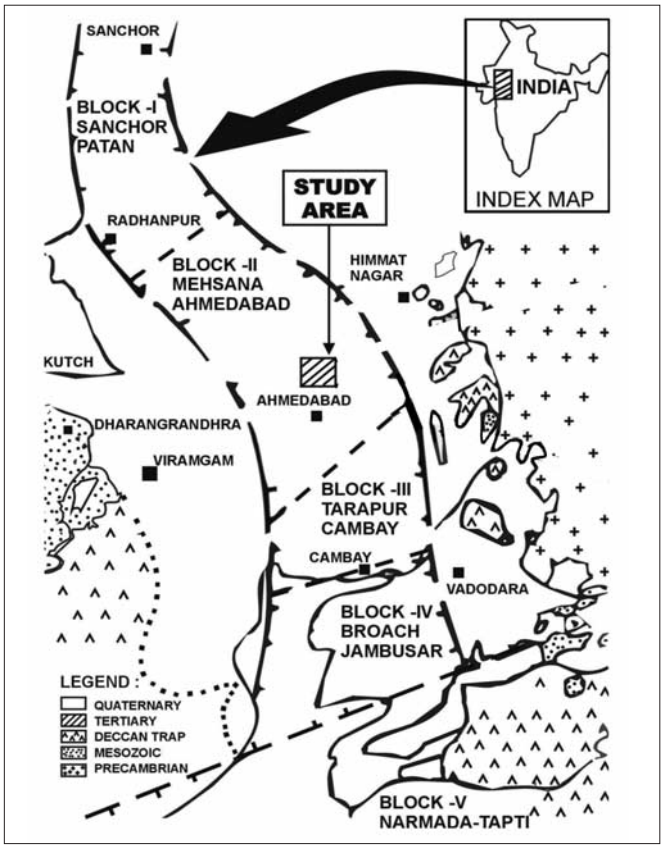

Figure 1. Map of Cambay Basin indicating the study area. The basin has produced commercial hydrocarbons from a variety of different blocks since the first discovery of oil in 1958.

indicate that the Cambay shale is the main source rock. The hydrocarbon index for the Cambay shale ranges from 40 to 316 mgHC/gTOC and maturity is in the early stage of catagenesis (VR_o< 0.8%).

The sands of the Middle Eocene Kalol Formation, the main reservoir rocks, typically represent channel mouth bars, point bars, crevasse splays, etc. Kalol Formation was deposited in a complex deltaic environment by distributary channels influenced by tides and also having marshy and swampy environments marked by coal, shale, sand, and silt units. The thickness of Kalol Formation in the area covered by 3D seismic ranges from 200 to 300 m. The overlying shale sections on the top of these sands act as a seal for hydrocarbon entrapment.

Stacked pay sand reservoirs of Kalol Formation at a depth of 1300–1600 m are the main hydrocarbon producers in the area covered by the 3D data and still hold a significant amount of hydrocarbons. Individual sandstone reservoirs are thin (thickness of 2–14 m), discrete, isolated, exhibit

Downloaded 12/28/14 to 129.105.215.146. Redistribution subject to SEG license or copyright; see Terms of Use at http://library.seg.org/

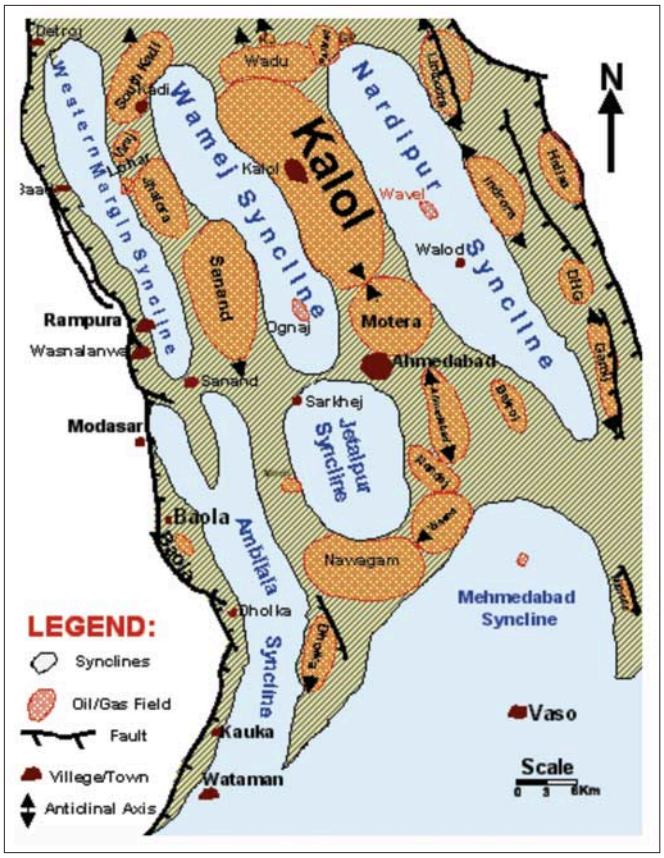

Figure 2. *Diagram of Mehsana-Ahmedabad block showing NW–SE anticlinal and synclinal features.*

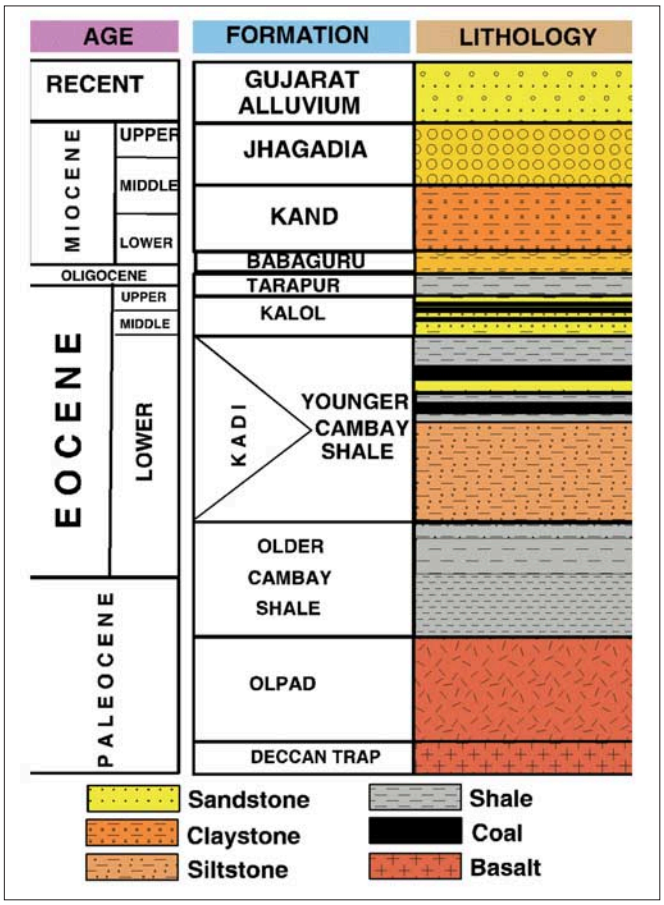

Figure 3. *Generalized stratigraphy of Cambay Basin.*

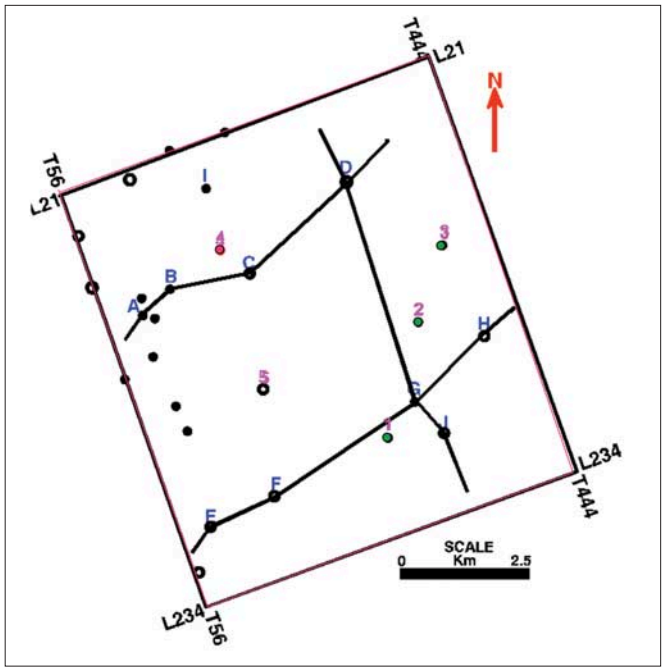

Figure 4. *Map indicating the area covered by 3D data, drilled wells, and profiles passing through wells A-B-C-D (SW–NE), E-F-G-H (SW–NE), and D-G-J (N–S). Black circles = producing wells; hollow circles = dry wells. Wells 1–5 were drilled after this study.*

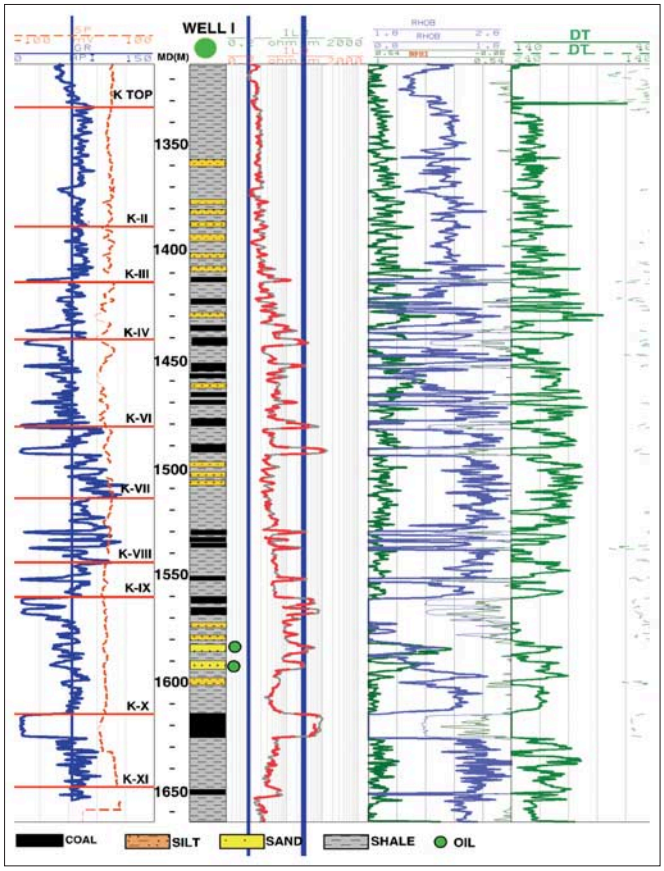

Figure 5. *Sample logs of well I showing signatures for different lithologies in Kalol Formation. They are (left to right) gamma ray in blue, SP in red, induction log (ILD) in red, neutron porosity (NPHI) in green, density (RHOB) in blue, and sonic transit time (DT) in green. Note that different coal units generate distinct responses (low GR, high resistivity, low density, relatively higher porosity, and sonic transit time).*

Downloaded 12/28/14 to 129.105.215.146. Redistribution subject to SEG license or copyright; see Terms of Use at http://library.seg.org/

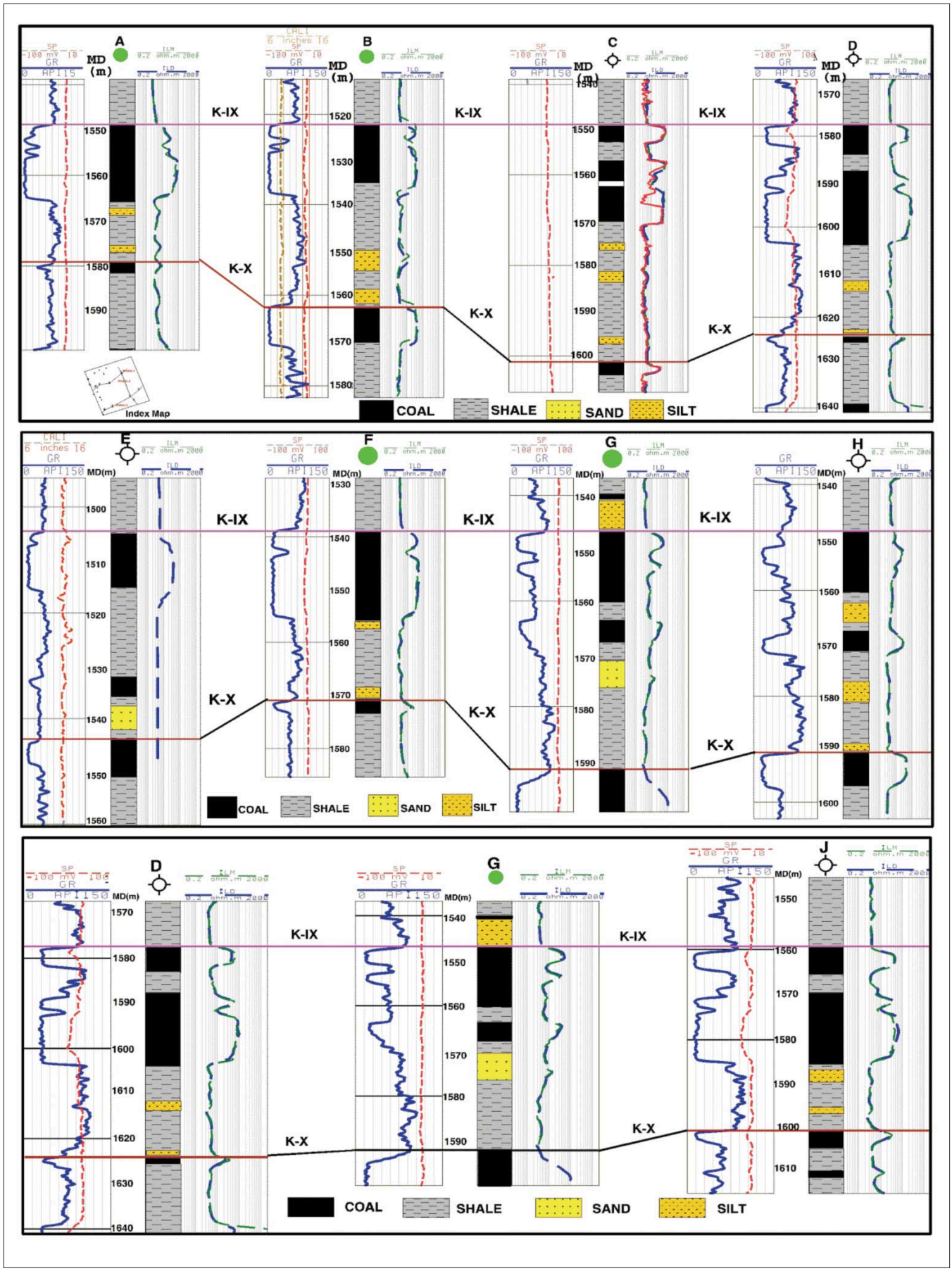

Figure 6. Log correlation profiles through wells A-B-C-D (SW–NE), E-F-G-H (SW–NE), and D-G-J (N–S) showing discrete sands in the K-IX unit of Kalol Formation.

Downloaded 12/28/14 to 129.105.215.146. Redistribution subject to SEG license or copyright; see Terms of Use at http://library.seg.org/

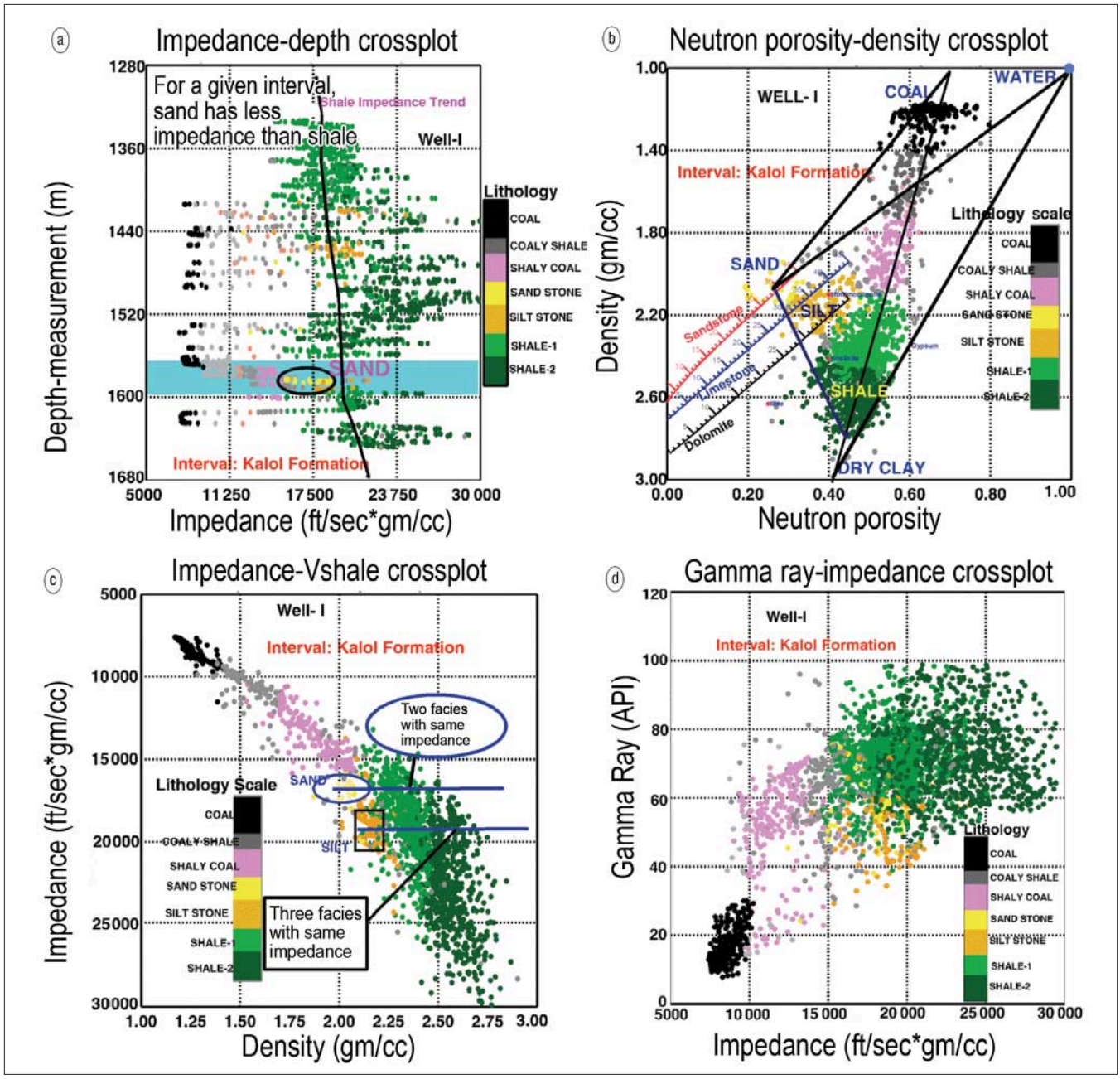

*Figure 7. Crossplot analysis at well I for Kalol Formation between (a) impedance and depth, (b) neutron porosity and density, (c) density and impedance, and (d) impedance and gamma ray. The sand zone, light blue in (a), has intermediate impedance values between coals and shales. Coals stand out clearly because of low density (1.2–1.4 gm/cc) and high neutron porosity values (0.5–0.8). The triangle formed by coal, sand, and shale (b) shows a lithological variation within the triangle from one lithology to another. There are no points along the sand-coal line within the triangle, which suggests an absence of a lithology transition from sand to coal. The variation in lithology between shale and coal is demonstrated by the shale-coal line. This line shows the variation of coal in shale (i.e., the lithology is coaly shale or shaly coal). Another triangle formed by the sand, shale and water points in (b) represents the variation of lithology and porosity. The sand-shale line shows the lithology variation of sand and shale and water-shale line to that of porosity. The variation in clay-bound water in shale is controlled by shale-water line. The impedance range of sand is 15 500–18 000 ft/sec*gm/cc and shales is 17 500–21 000 ft/sec*gm/cc. The impedance of coal is always less than 10 000 ft/sec*gm/cc.*

intricate geometries with limited areal extent, and are sandwiched between coal and shale layers. These sands are susceptible to tuning and therefore the upper and lower interfaces may not be independently resolved on the seismic data. Apart from their discrete nature, internal lithological heterogeneity within the reservoir has affected the porosity distribution. Low-porosity zones are devoid of hydrocarbons. Initial exploratory efforts concentrated on structural prospects. Two recent exploratory wells, one in the rising flank and the other in the central part of the Nardipur syncline, have encountered hydrocarbon-bearing porous reservoir sands in Kalol's K-IX unit. This has generated further interest in stratigraphic, combination, and nonconventional traps on the flanks of anticlines and in the central part of the synclines.

Data base. 2D seismic data of various vintages and fold cover the study area. However, these attempts to map the producing reservoirs of Kalol Formation did not succeed because of the sparseness of the data sets and the thin sands with varying geometries. 3D seismic data were later acquired over 70 km^2. A bin size of 20 × 40 m was adopted for record-

Downloaded 12/28/14 to 129.105.215.146. Redistribution subject to SEG license or copyright; see Terms of Use at http://library.seg.org/

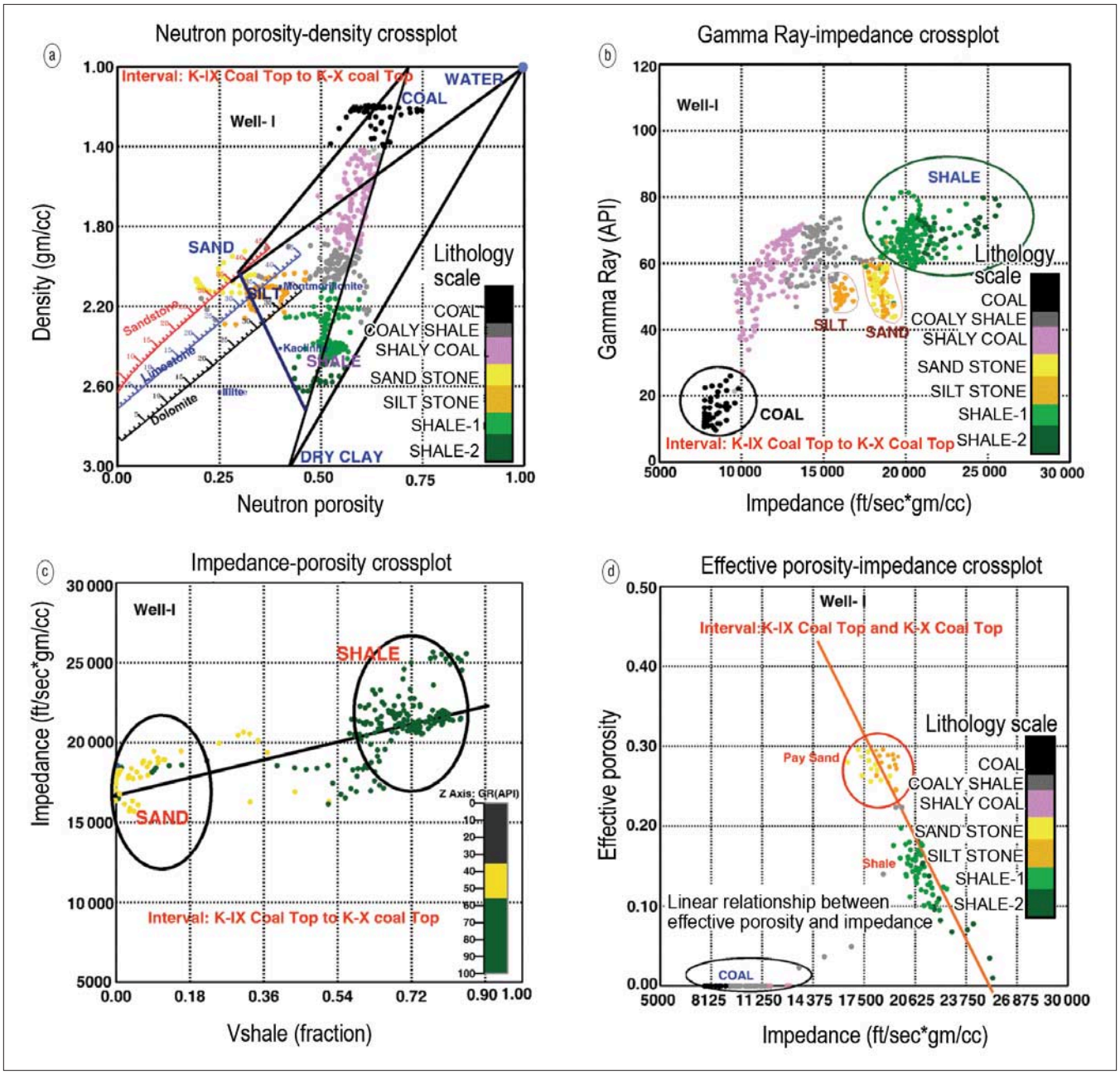

Figure 8. Crossplot analysis at well I for K-IX unit between (a) neutron porosity and density, (b) impedance and gamma ray, (c) V_{shale} and impedance, and (d) effective porosity and impedance. The triangles shown in neutron porosity versus density plot have a similar interpretation as discussed in Figure 7. The plot between Vsh and impedance shows the linear increase of impedance values with increasing Vsh. The plot between impedance and effective porosity shows a linear relationship determining the impedance range corresponding to reservoir sand.

ing 35-fold seismic data with a sampling interval of 2 ms. A standard 3D processing sequence was used, including surface-consistent static corrections, amplitude balancing, deconvolution, velocity analysis with a 480 × 500 m grid, dip moveout corrections, and one-pass finite-difference migration in the *f-x* domain. The dominant frequency of the final migrated data volume is in the range of 37–42 Hz at the zone of interest (1.0–2.0 s). The interpretation included analysis of the migrated 3D seismic data volume, wireline logs from 30 wells (generally including gamma ray, resistivity, SP, neutron porosity, sonic, and density), geologic and engineering information, core data, and well-test results. Figure 4 shows the area covered by 3D seismic data, drilled wells and profiles passing through wells A-B-C-D (SW–NE), E-F-G-H (SW–NE) and D-G-J (N–S).

Workflow. An advanced quantitative methodology integrating 3D seismic, well logs, and geologic information was adopted. The interpretation steps include well-log signature, correlation and petrophysical analysis, calibration of seismic with well-log data, horizon correlation, structural mapping, stratigraphic analysis using window-based amplitude attributes, spectral decomposition, and acoustic impedance inversion. To analyze the lateral variations of reservoir properties away from the boreholes and in interwell regions, it was necessary to integrate reservoir properties derived from core and log data with seismic attributes. This was attempted when estimating the effective porosity of the producing reservoirs using supervised neural networks. These steps will be described in detail.

Downloaded 12/28/14 to 129.105.215.146. Redistribution subject to SEG license or copyright; see Terms of Use at http://library.seg.org/

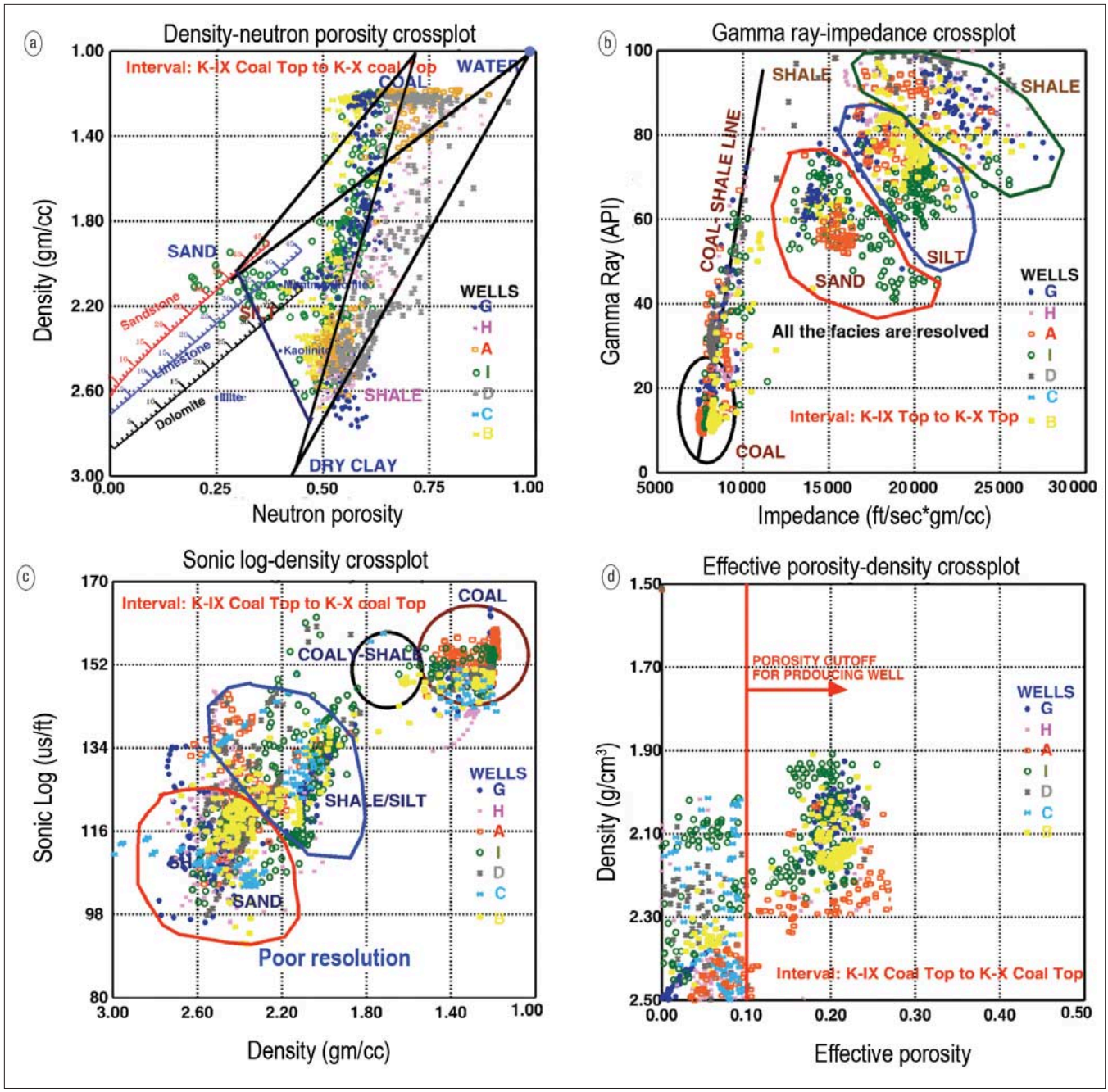

Figure 9. Crossplot analysis at wells A, B, C, D, G, H, and I for K-IX unit between (a) neutron porosity and density, (b) impedance and gamma ray, (c) density and sonic transit time, and (d) effective porosity and density. The triangles shown in the neutron porosity versus density plot have a similar interpretation as discussed in Figures 7 and 8. The cutoff porosity for producing reservoir is 10%.

Well-log signature, correlation, and petrophysical analysis. The recorded suite of logs can be grouped into two categories: properties that affect seismic-wave propagation in the subsurface (e.g., compressional- and shear-velocity logs and density log) and properties of interest for reservoir description but which do not directly affect seismic-wave propagation (e.g., porosity, water saturation, and clay content). Petrophysical analysis through conventional crossplots is the key to relating the two groups. Logs were carefully edited to compensate for washouts, cycle skipping, environmental corrections, and any other problems. Selected logs from well I (Figure 5) show the responses from different lithologies of Kalol Formation.

Kalol Formation consists of coal, shale, silt, and sandstone layers. The coals are represented by high resisitivity, low gamma, low density, and relatively higher porosity and sonic traveltime. These distinct responses of coal units allow Kalol Formation to be divided into 11 units, K-I to K-XI (from top to bottom). The thickness of the coal units varies from 2 to 32 m in the study area. The thickness of individual sand units varies from 2 to 14 m. The sands in K-IX, the main hydrocarbon producers, are represented by relatively high resistivity and low gamma ray when compared with overlying or underlying shales and show crossover in the density-neutron porosity logs. The resisitivity of producing sands varies from 2 to 7 ohm-m. Effective porosity of these reservoirs is 20–24%. Log correlation profiles passing through wells A-B-C-D (SW–NE), E-F-G-H (SW–NE), and D-G-J (N–S) after flattening at K-IX top are shown in Figure 6.

Downloaded 12/28/14 to 129.105.215.146. Redistribution subject to SEG license or copyright; see Terms of Use at http://library.seg.org/

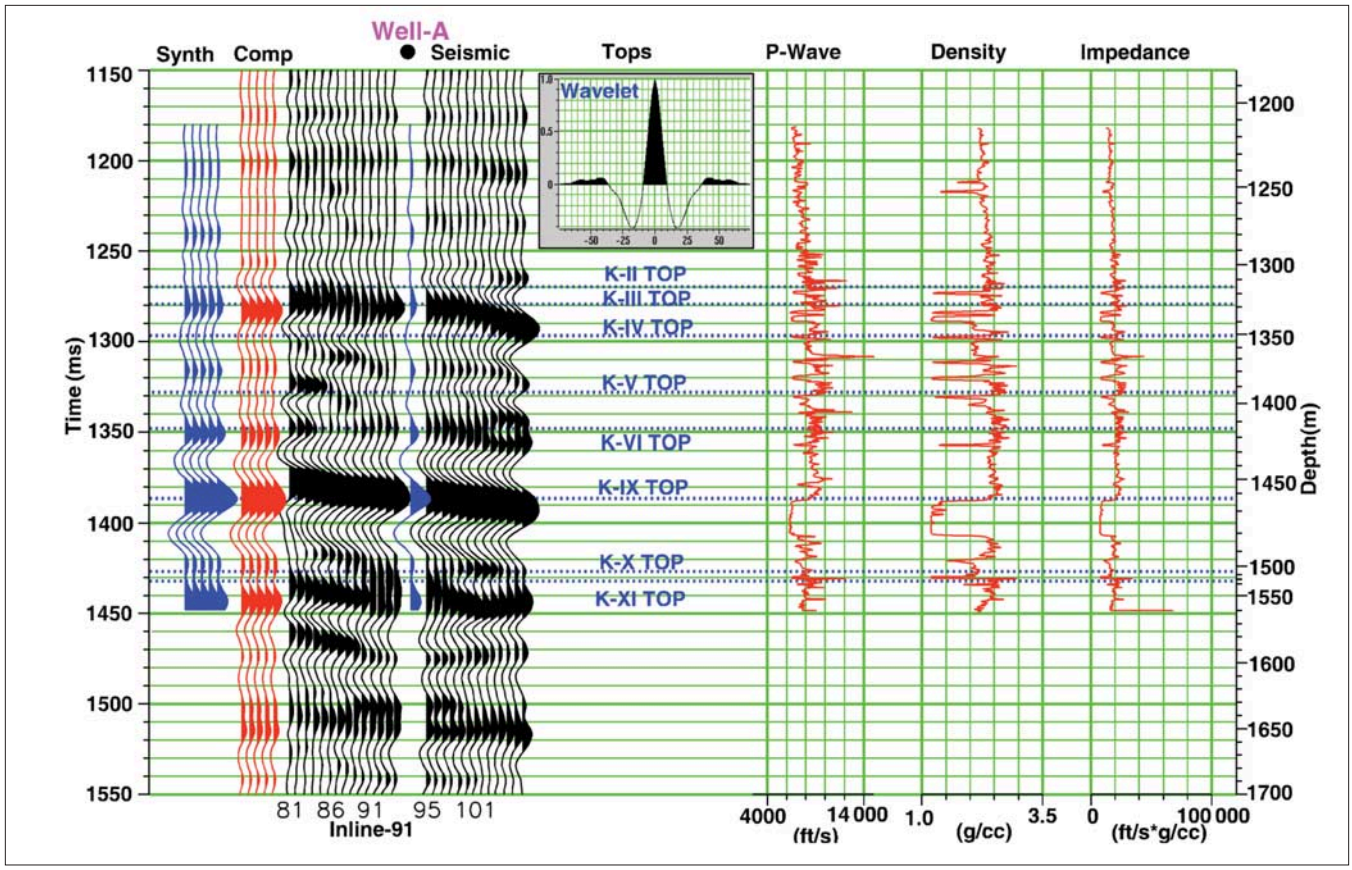

Figure 10. *Calibration of surface seismic with synthetic seismogram and log data at well A. A synthetic trace (blue) generated from the well-log data is inserted at the well location in the real seismic. Correlation between synthetic and real seismic is 0.9024. Composite traces (red) are generated by averaging five traces nearest to the well.*

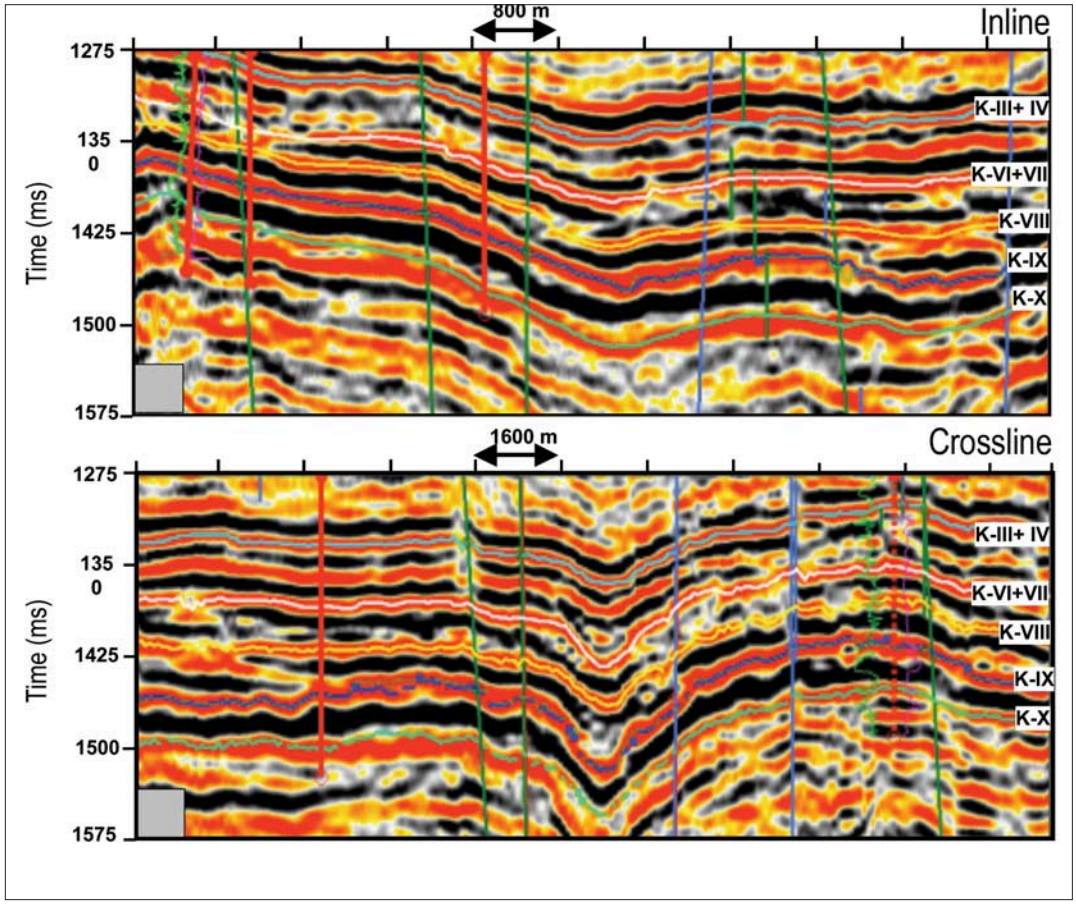

Figure 11. *Representative inline and crossline sections from 3D data volume showing tracked horizons.*

Downloaded 12/28/14 to 129.105.215.146. Redistribution subject to SEG license or copyright; see Terms of Use at http://library.seg.org/

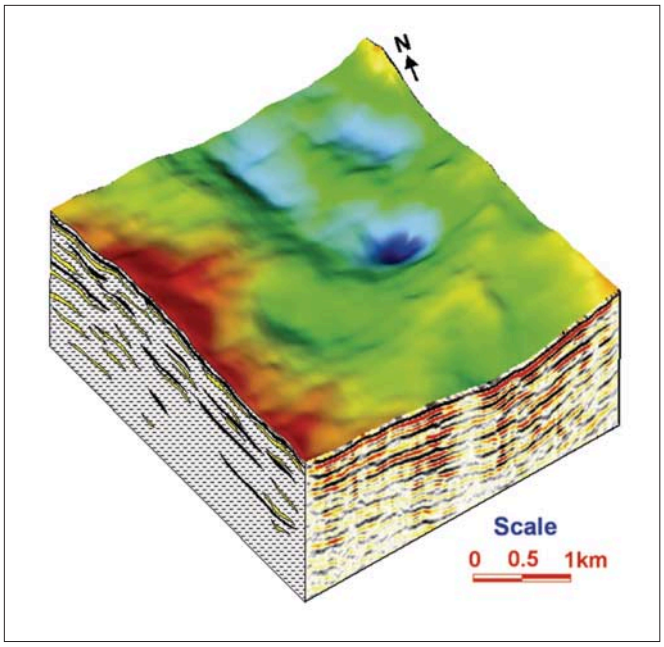

Figure 12. 3D view of time structure map at the top of K-IX coal, along with seismic inline section and crossline seismo-geological section. Structural highs are red and lows are blue.

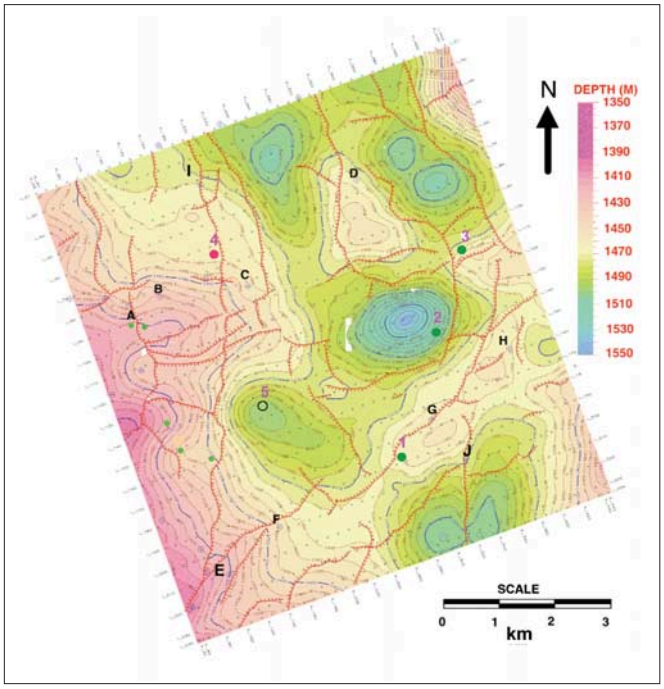

Figure 13. Depth structure contour map corresponding to K-IX top. Contour interval is 5 m. Structural highs are red and lows are blue. N–S and E–W trending faults generate different fault blocks, which are important for hydrocarbon entrapment.

Extensive petrophysical analysis of the various rock data within Kalol Formation and their relationship to lithology, porosity, and fluid types was carried out in three steps. In the first step, the total Kalol interval was taken at well I and plots between impedance and depth, neutron porosity and density, density and impedance, and impedance and gamma ray were generated (Figure 7) to understand the variation of different lithologies. These plots suggest that only coal can be uniquely identified. Other lithologies are not identifiable because of variations of porosity, clay content within

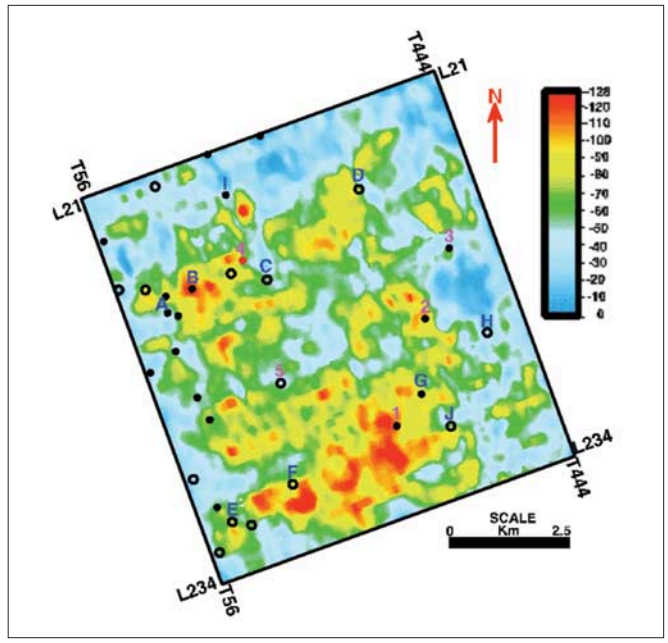

Figure 14. Average negative amplitude map of K-IX sands. Sand distribution geometry is not well defined due to limited seismic resolution.

the sand, silt, and the effect of overburden pressure on shales. In the second step, a small window between the top of the K-IX coal and the top of the K-X coal was chosen for further analysis.

Plots between neutron porosity and density, impedance and gamma ray, V_{shale} and impedance, and impedance and porosity were generated (Figures 8). Effective porosity (the porosity available for water or hydrocarbon in the rock) is computed by taking a linear average of shale-corrected density-porosity and shale-corrected neutron-porosity. When computing the effective porosity, the thickness and porosity of coal were not taken into account. The plot between impedance and V_{shale} shows a linear increase of impedance with increasing V_{shale}. The plot between impedance and effective porosity shows a linear relationship determining the impedance range corresponding to reservoir sand. Finally, in the third step, in order to understand the finer details of the hydrocarbon-bearing zones, other lithologies and their relationship with seismic signature, seven wells (A, B, C, D, G, H, and I) were analyzed. Plots were generated for neutron porosity and density, impedance and gamma ray, density-sonic transit time, and impedance and effective porosity and density. These plots (Figure 9) indicate that sand, shale, and coal facies are clearly separable in the smaller interval (K-IX unit) and that effective porosity plays a crucial role in hydrocarbon accumulation in this area.

Well-to-seismic calibration and structural mapping. Sonic and density logs were available for 12 wells and were used for generating synthetic seismograms. The time-depth curves generated from the VSP data were also incorporated. In the processed data volume, an increase in impedance is represented by negative reflection amplitude and is plotted as a trough. Synthetic seismograms generated from sonic and density logs show that the tops of different coal units in Kalol generate distinct peaks which have been used for horizon correlation after a proper well-to-seismic tie. Figure 10 displays the calibration of seismic data with well logs using synthetic seismograms at well location A. A composite wavelet was extracted using both seismic and available

Downloaded 12/28/14 to 129.105.215.146. Redistribution subject to SEG license or copyright; see Terms of Use at http://library.seg.org/

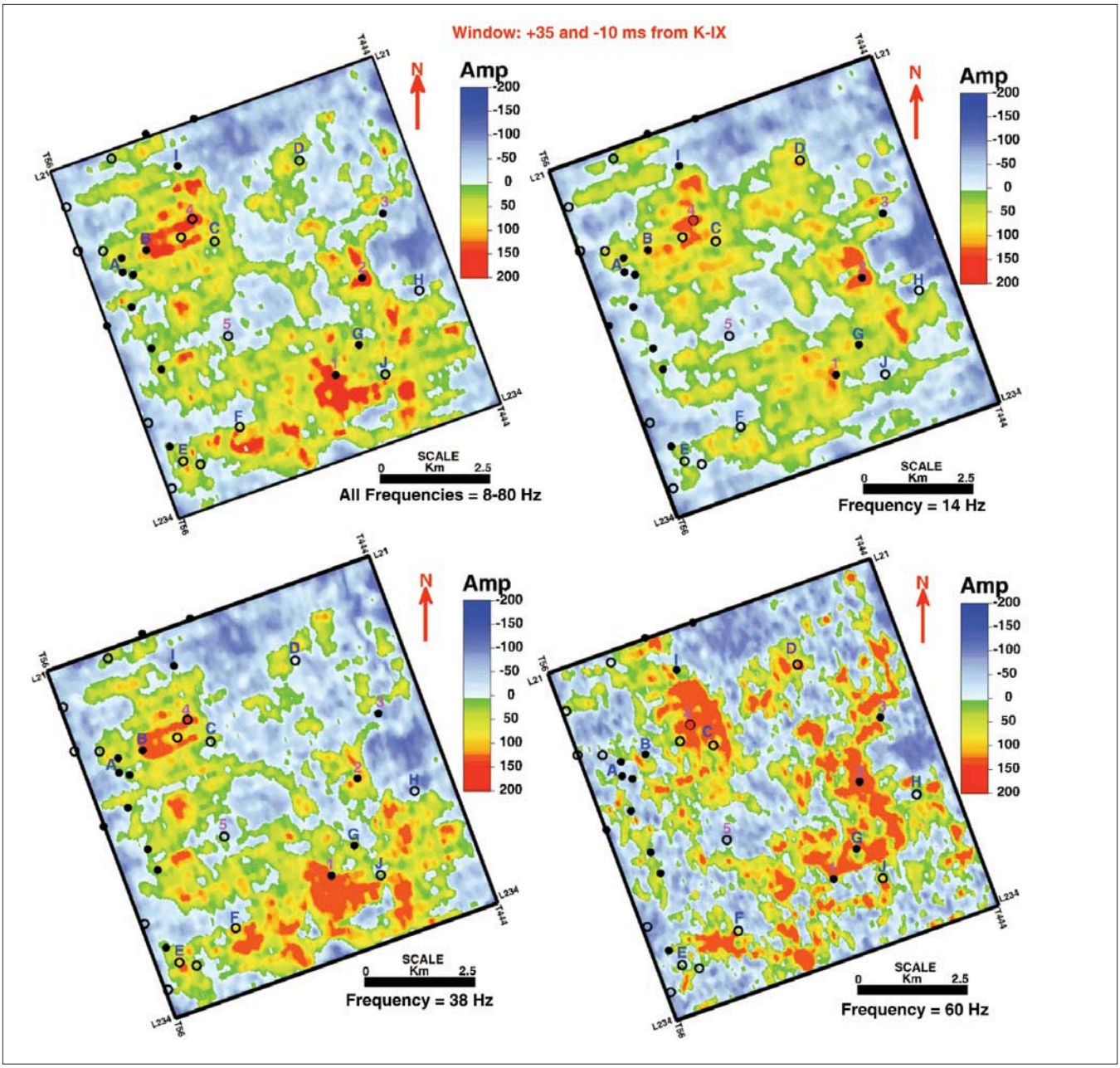

Figure 15. Spectral decomposition analysis for different mono frequencies to infer reservoir geometry and sand thickness. The amplitude maps corresponding to 38 and 60 Hz indicate separate channel features in the western and eastern part of the 3D study area.

well logs in the study area and the 3D seismic data were processed to achieve zero phase, to maximize the resolution by broadening the bandwidth, and to improve the tie between the seismic and well-log data. Several horizons (namely K-top, K-III, K-VI+VII, K-VIII, K-IX, and K-X) were correlated on the zero-phase 3D data volume. Representative of zero-phase inline and crossline sections from the 3D data volume are shown in Figure 11 along with correlated horizons. A 3D view of the time structure map corresponding to the K-IX top horizon along with a seismic inline section and a seismo-geologic section in the crossline direction are shown in Figure 12. The structural highs are red and lows are blue. The sand bodies within the different Kalol units, in general, follow the same structural trend as their unit boundaries. Figure 13 shows a structure map corresponding to the K-IX top horizon that was prepared using a 3D velocity grid and VSP data.

Stratigraphic analysis using window-based amplitude attributes, spectral decomposition, and acoustic impedance inversion. Delineation of stratigraphic prospects was difficult because of thin and discontinuous occurrences, a high degree of vertical and lateral variability in net thickness, and limited bandwidth of the seismic data. Consequently, interpretation involved integrating geologic and seismic data, drilling results, and available state-of-the-art interpretation tools. Seismic attributes derived from amplitude are extensively used to predict subsurface properties. In our case, because of the seismic resolution limits, the thin multipay sands of the K-IX unit are not resolved. A composite response is embedded in the trough (negative amplitude) and at times is affected by the overlying K-IX coal. The average negative amplitude attribute map of the K-IX sands with an 18-ms window corresponding to the trough was prepared (Figure 14). This amplitude map does not provide any well-defined

Downloaded 12/28/14 to 129.105.215.146. Redistribution subject to SEG license or copyright; see Terms of Use at http://library.seg.org/

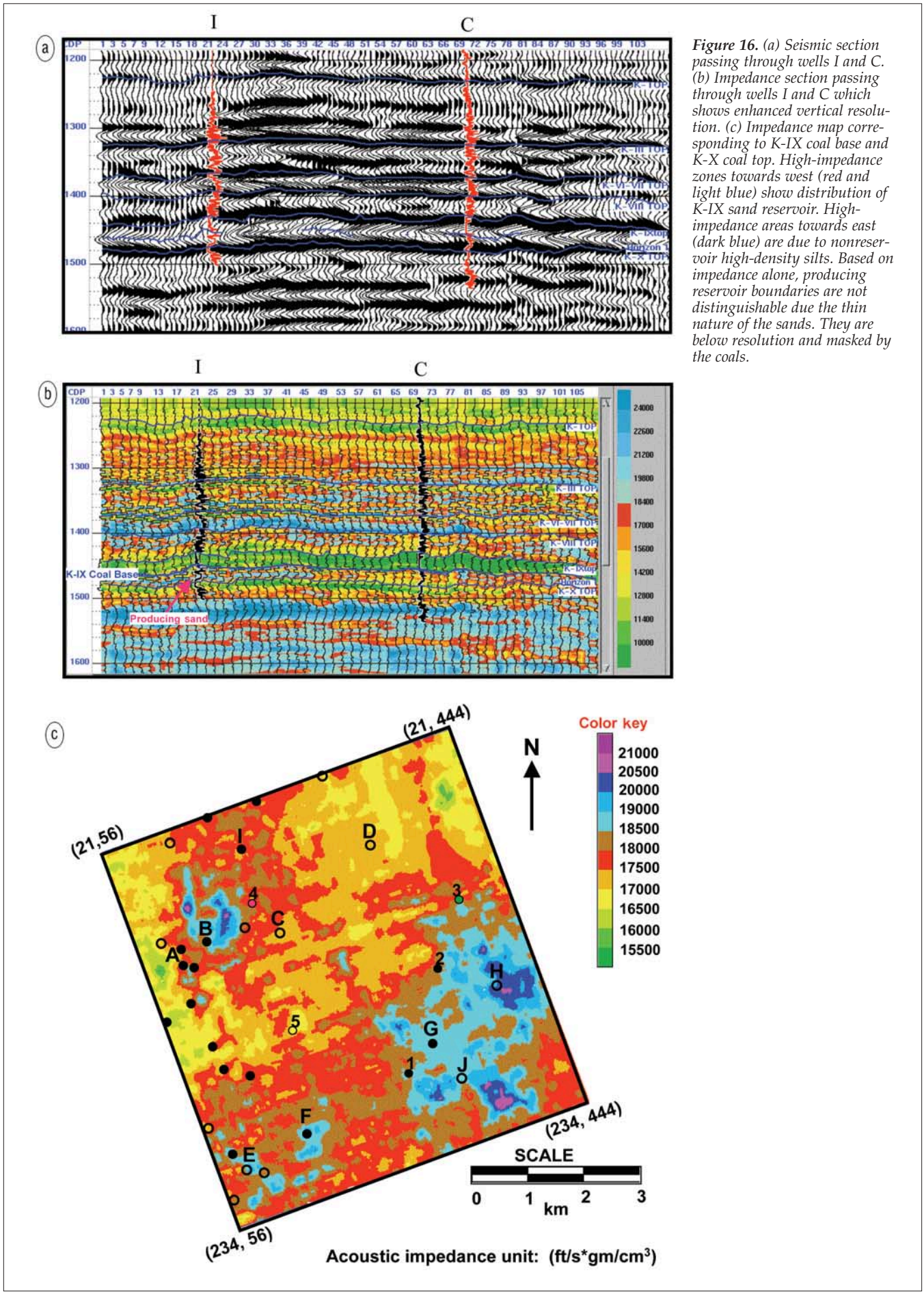

Figure 16. *(a) Seismic section passing through wells I and C. (b) Impedance section passing through wells I and C which shows enhanced vertical resolution. (c) Impedance map corresponding to K-IX coal base and K-X coal top. High-impedance zones towards west (red and light blue) show distribution of K-IX sand reservoir. High-impedance areas towards east (dark blue) are due to nonreservoir high-density silts. Based on impedance alone, producing reservoir boundaries are not distinguishable due the thin nature of the sands. They are below resolution and masked by the coals.*

Downloaded 12/28/14 to 129.105.215.146. Redistribution subject to SEG license or copyright; see Terms of Use at http://library.seg.org/

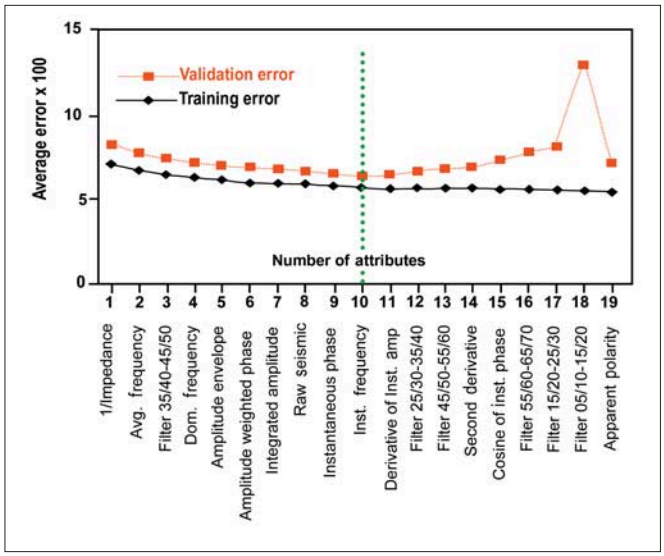

Figure 17. Multi-attribute stepwise linear regression analysis using 19 attributes at eight wells. Green dotted line shows that at 10 attributes, the validation error is minimum. With a further increase in attributes, the validation error increases. Thus, because of the minimum validation error, 10 attributes were chosen for further analysis.

reservoir geometry distribution.

In order to delineate thin reservoirs below seismic resolution, spectral decomposition was used to transform time-domain seismic data into frequency-domain. The reflected seismic waveforms in the zone of interest were reprocessed through discrete Fourier transforms (DFT) to show their frequency characteristics. Figure 15 shows amplitude maps for different frequencies. The maps corresponding to frequencies of 38 and 60 Hz indicate separate channel features in the western and eastern part of the 3D study area.

In an attempt to delineate the K-IX producing sands more precisely and to remove the effect of coal, a model-based stratigraphic inversion was carried out combining the zero-phase 3D data volume, well logs, and interpreted horizons. Calibration with the geologic information appears to have enhanced the vertical resolution and identification of the pay sands improved in the inverted volume (Figures 16a and 16b). Figure 16c, an impedance map corresponding to a window between K-IX coal base and K-X coal top, shows the distribution of the sands and shale facies within this window but does not clearly explain the distribution of producing reservoirs.

Effective porosity estimation using probabilistic neural networks. The porosity distribution was predicted (using effective porosity logs, various seismic attributes extracted from 3D data, and the impedance volume) by a combination of stepwise regression and artificial neural network techniques. A multi-attribute stepwise linear regression analysis was performed at eight wells using 19 sample-based attributes (Figure 17), including acoustic impedance as an external attribute. A seven-point convolution operator was used. The average rms training error was computed with all wells taken into consideration. The validation error was computed by hiding one well at a time. The training error reduces with an increasing number of multi-attribute transforms. However, the validation error decreases for 10 attributes and then again increases as more attributes are added. Therefore, a multi-attribute transform using 10 out of 19 various sample-based attributes was selected to generate pseudo-effective porosity logs.

Figure 18a shows a plot between actual and predicted effective porosity values using points from the analysis windows of all eight wells. The correlation coefficient for the linear regression using 10 attributes is 0.65728, with an average error of 0.051416. This plot shows that the multi-attribute transform model using stepwise linear regression has a tendency to overpredict the lower porosities and to underpredict the higher porosity values. The application of the multilinear regression method has modeled the effective porosity curve but it has failed to pick the extreme values in the predicted curve. To further reduce the error between actual and predicted effective porosities and to determine the nonlinear relationships, this trained and validated multiattribute transform of 10 attributes (Figure 17) was used to train the probabilistic artificial neural networks (PNN).

After training the PNN, a plot of predicted porosity values against actual porosity values using points from the analysis windows of all eight wells was generated (Figure 18b). The scatter is minimal and data points much closer to the regression line as compared to the multilinear regression case. This PNN technique provided a better correlation coefficient (0.871709) between actual and predicted effective porosity with an average error of 0.0338822. The application of PNN using 10 attributes clearly shows the advantage over the multi-attribute linear regression as the predicted effective porosity logs are very close to the actual logs in the target zone (Figure 19a). By hiding one well at a time, the results of PNN were validated; this resulted in a cross-correlation coefficient of 0.643832 with an average error of 0.053327 (Figure 19b). The PNN-based prediction of effective porosity retains more dynamic range and high-frequency content because the PNN result is a nonlinear function and closely follows the training or the control data. The trained model of the PNN was used to create a porosity volume from seismic data and from this the effective porosity map corresponding to the K-IX sands was generated (Figure 20).

Results and discussion. The extensive crossplot analysis carried out using well-log data for the entire Kalol Formation and for the selected interval between K-IX top coal and K-X top coal has been very helpful in providing the relationships between seismic parameters, acoustic impedance, velocity and density. This analysis has been useful in differentiating the lithologies, reservoir and nonreservoir facies, and establishing the relationship between reservoir properties and each acoustic property. The plot of effective porosity against bulk density has shown that effective porosity plays a key role in hydrocarbon production in K-IX reservoirs of this area.

The structure map at the top of K-IX coal shows that a well-defined NW–SE central low exists at the K-IX level. This low is bounded by N–S faults on both sides having differential fault throws, which makes the central portion the deepest part. The rising flanks of Kalol Field in the western part of the 3D area show E–W nosing features that are dissected by N–S and E–W faults which give rise to different fault blocks. Another important structural feature at the K-IX level is the ENE–WSW horst, which passes through wells F, G, and H and is bounded by parallel faults on both sides. These structural trends have played an important role in hydrocarbon entrapment.

The window-based seismic amplitude map generated from average trough value does not explain the sand geometry adequately because this amplitude does not represent the sole contribution from sands. In places, it is affected by the presence of thick overlying K-IX coal and is a compos-

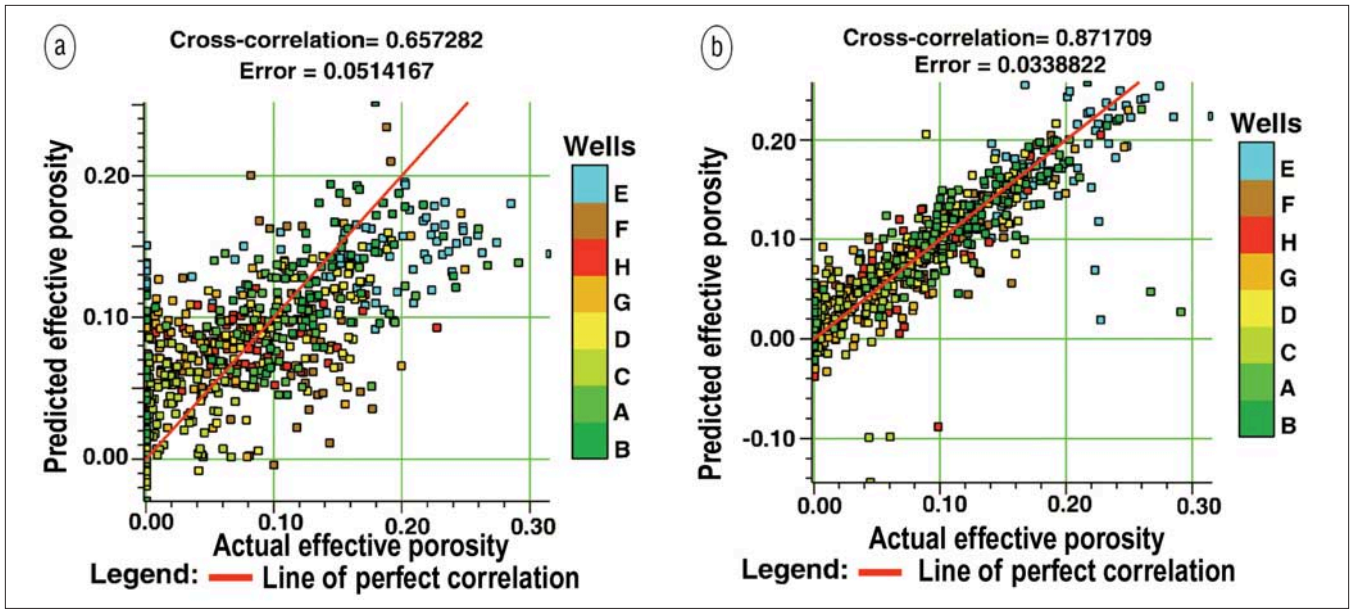

Figure 18. Plot between actual and predicted effective porosity for 10 attributes using (a) multi-attribute transforms and (b) probabilistic neural networks. Data points from analysis window of each well are shown in one color. The crossplot for multilinear regression shows the tendency to overpredict at lower and underpredict at higher actual porosities. The scatter in the data increases. In the case of PNN, the scatter is minimal and data points are very close to the regression line.

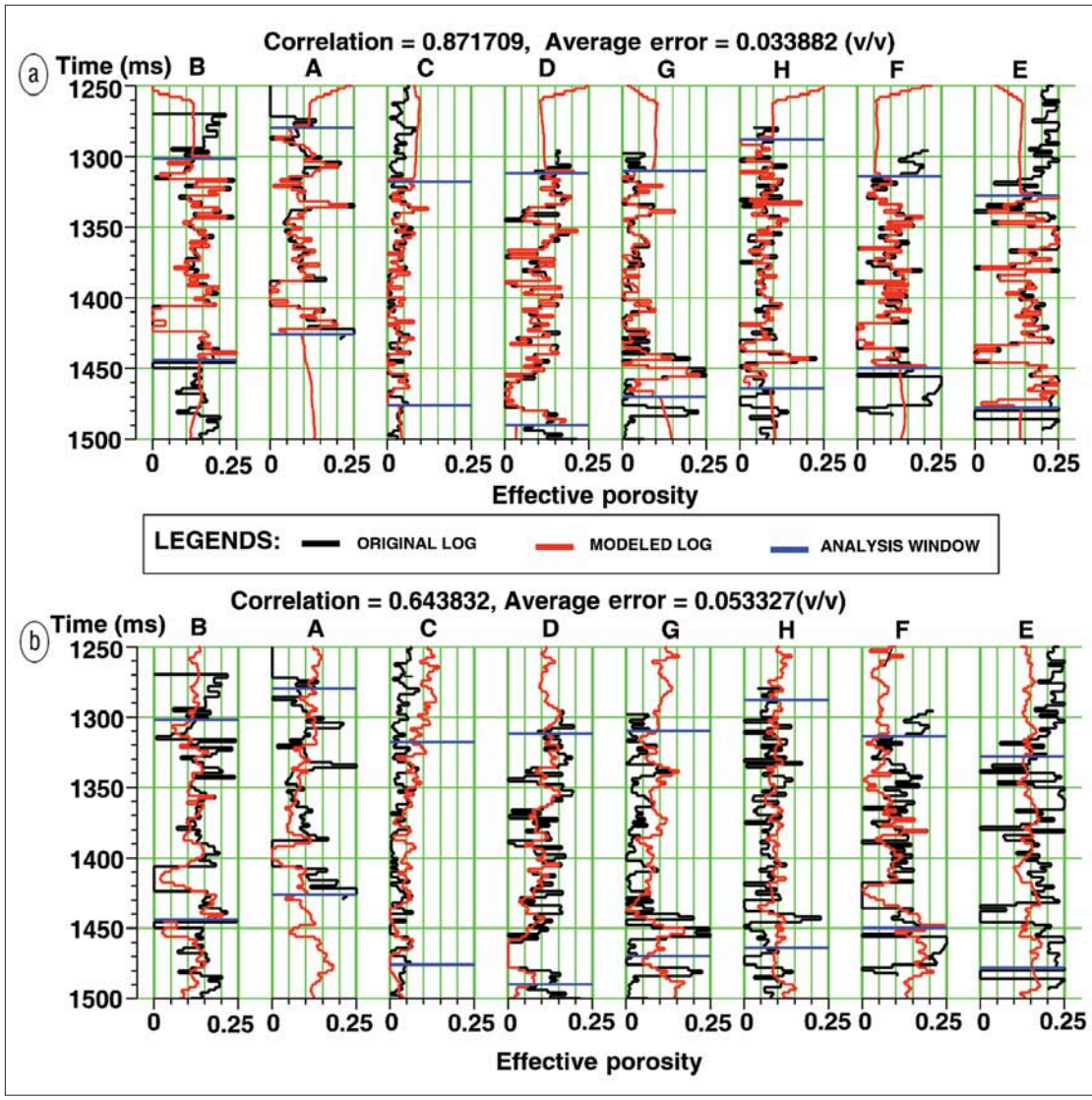

Figure 19. (a) Application of probabilistic neural networks using 10 attributes to predict the effective porosity of K-IX sands. (b) Validation of probabilistic neural networks using 10 attributes. Modeled log at each well is predicted by hiding it from the analysis. These results show the efficacy of predicting the effective porosity of K-IX sands.

Downloaded 12/28/14 to 129.105.215.146. Redistribution subject to SEG license or copyright; see Terms of Use at http://library.seg.org/

Downloaded 12/28/14 to 129.105.215.146. Redistribution subject to SEG license or copyright; see Terms of Use at http://library.seg.org/

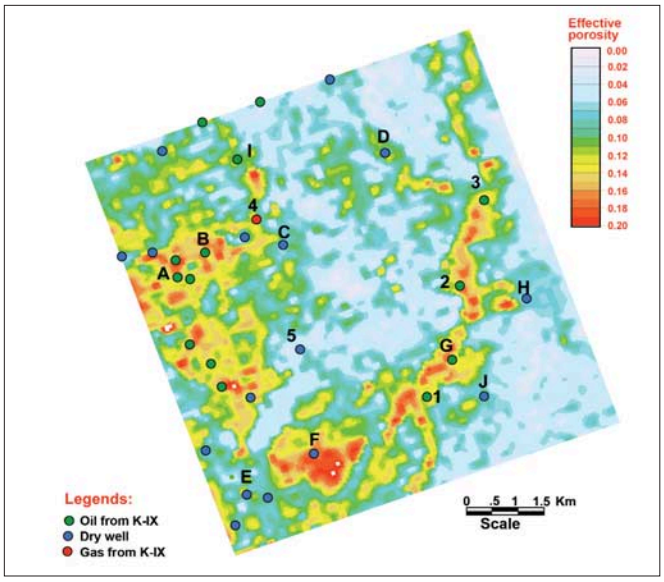

Figure 20. Effective porosity map of K-IX sands using probabilistic neural networks with 10 attributes. This map shows that producing reservoirs are discrete in nature.

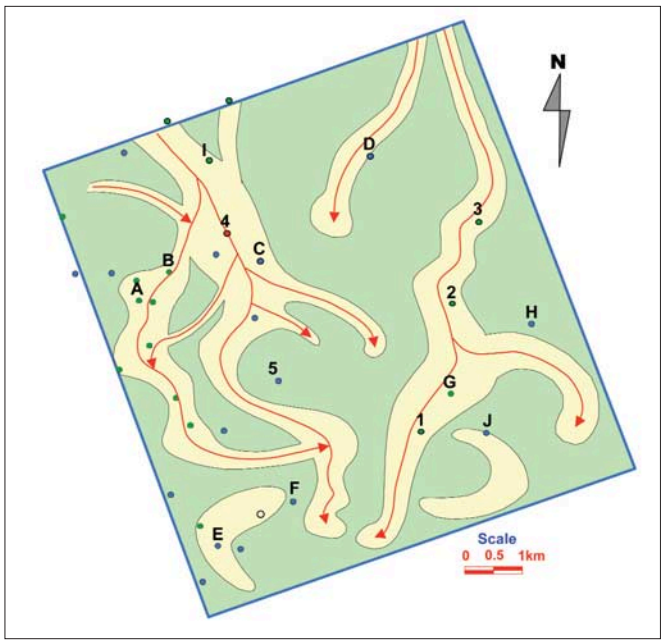

Figure 21. The geologic model for the distribution of channel-filled K-IX sands. The arrow indicates the channel flow direction.

ite response. Frequency amplitude maps obtained from spectral decomposition were very useful in delineating thin reservoirs below the conventional quarter wavelength resolution limit. Lower frequencies were able to delineate thicker sand-prone areas and higher frequencies thinner ones. The amplitude maps at discrete frequencies display the distribution of the fluvial channel-filled sands and also reveal the evolution of the channel system through time. Model-based poststack seismic inversion has enhanced the vertical resolution and minimized the tuning effects. This has been very useful in obtaining layer-by-layer information of sand units and hence a lithostratigraphic interpretation. This map shows that the K-IX sands are distributed in the northwestern part while, in the eastern part, very high-impedance areas are due to presence of silts. These maps explain the presence of sand

Table 1. *Reservoir parameters of five postdrilled wells.*

	Reservoir sand	Pay thickness (m)	Effective porosity ϕ (%)	Shale volume (%)	Water saturation S_w (%)
Well 1	K-IX	6	18–20	24	20
Well 2	K-IX	8	21–22	22	15
Well 3	K-IX	5	18	25	10
Well 4	K-IX	3	22	28	15
Well 5	K-IX	3	12	40	44

but fail to explain the hydrocarbon entrapment.

In order to explain hydrocarbon presence or absence, the effective porosity was estimated. Deriving a deterministic relationship between the seismic data and effective porosity is difficult. The standard statistical methods (least squares, partially least squares, step-wise linear regression) were not useful as the relationship between the effective porosity and seismic attributes is not linear. To address the nonlinear and complicated relationship between effective porosity and multi-attribute transforms, probabilistic neural networks were used to generate a predicted effective porosity volume. The predicted effective porosity map is more precisely defined and explains the well results and matches the extremes of the porosity values. The low-porosity patches between the high-porosity zones are clearly demarcated. The lateral effective porosity variation clearly highlights the porous and nonporous zones in this stratigraphically controlled reservoir and honors the well data. By combining amplitude maps from different frequencies and the effective porosity map, it is possible to determine the distribution of channel-filled sands below the K-IX coal unit (Figure 21). Five wells, drilled based on this work, validate the predicted reservoir model (Figure 22). Four wells, drilled in channel features, were hydrocarbon-bearing. The one well drilled outside the channel is devoid of sand. Table 1 shows the reservoir parameters for these five wells. In addition, two successful development wells have also been drilled based on this work.

Conclusions. This study shows that a systematic, integrated interpretation approach combined with artificial neural network techniques helped in understanding the subsurface, and allowed precise mapping of reservoir sand geometries and internal reservoir properties. The ability of artificial neural networks to extract information from data and present it in a way that accentuates the features of interest allows more intelligent interpretations. Predicting effective porosity through supervised neural networks has provided a very high degree of confidence in analyzing the porous and nonporous zones of the reservoir. This study has been very helpful in providing more meaningful geologic information about the extent, shape and lateral lithological variation of reservoirs. It has explained hydrocarbon entrapment in the 3D study area in a more realistic way, thus reducing the cost of exploration and production and improving the recovery through more efficient production and better reservoir management, and has opened up new adjoining areas for further exploration.

Downloaded 12/28/14 to 129.105.215.146. Redistribution subject to SEG license or copyright; see Terms of Use at http://library.seg.org/

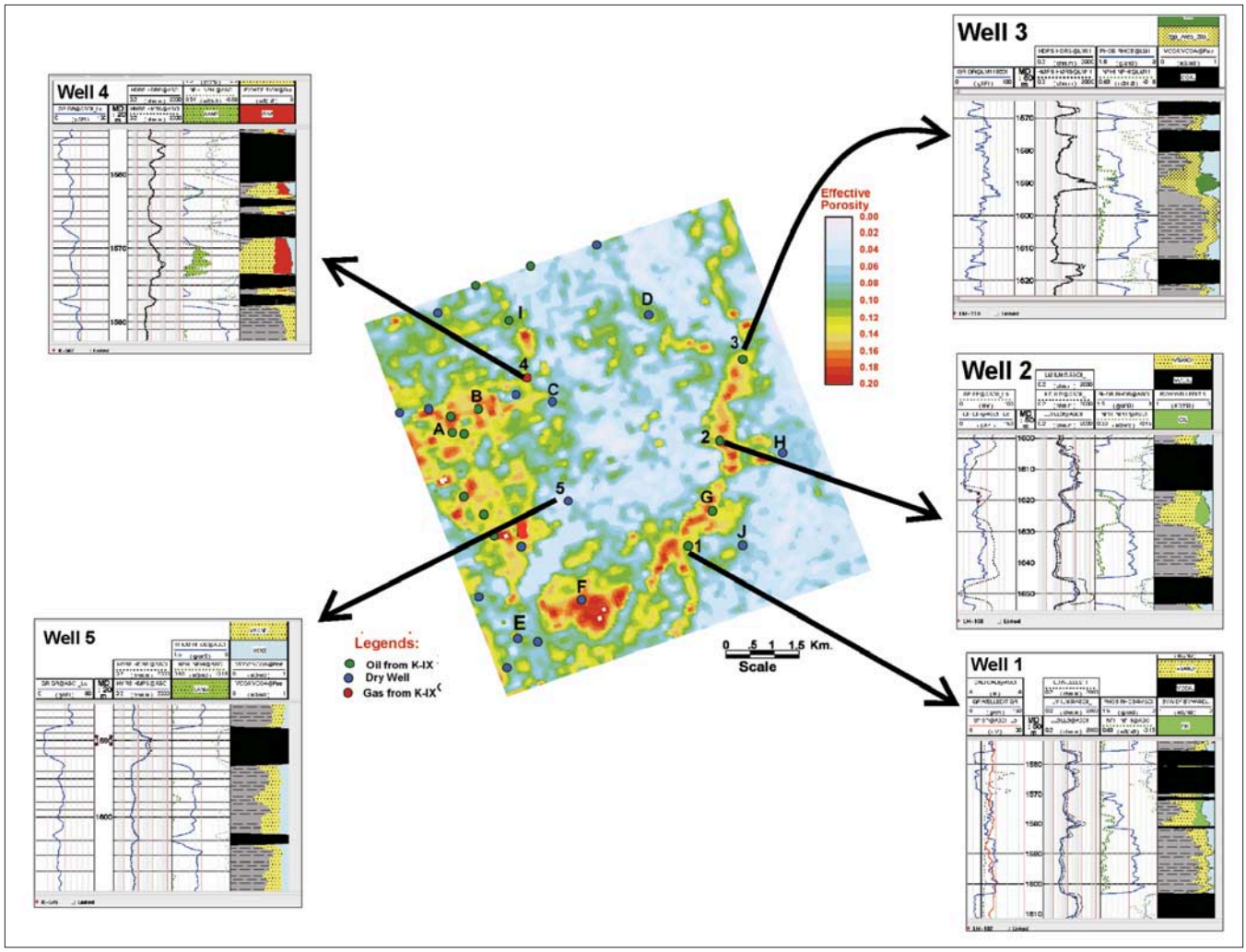

Figure 22. Diagram showing five wells and their log signatures at producing intervals along with effective porosity map of K-IX reservoir made prior to drilling these wells.

Suggested reading. "Petroleum systems in the Indian Sedimentary Basins: Stratigraphic and geochemical perspectives" by Chandra et al. (*Bulletin of the Oil and Natural Gas Corporation*, 2001). "Stratigraphic inversion for enhancing vertical resolution" by Pramanik et al. (*Geohorizons*, 2002). "Utilization of seismic attributes for reservoir mapping: a case study from Cambay Basin, India" by Srivastava et al. (*CSEG Recorder*, 2003). "Estimation of effective porosity using geostatistics and multi-attribute transforms: a case study" by Pramanik et al. (GEOPHYSICS, 2004). "Understanding the seismic resolution and its limit for better reservoir characterization" by Singh and Srivastava (*Geohorizons*, 2004). "A case study of stratigraphic and lithologic interpretation of thin reservoirs through an integrated approach" by Bose et al. (*TLE*, 2004). "Identification and delineation of subtle stratigraphic prospects by advanced interpretation tools: a case study" by Srivastava et al. (*TLE*, 2005). TLE

Acknowledgments: The authors are grateful to Oil and Natural Gas Corporation Limited, India for providing the facilities to carry out this work and for permission to publish this paper. All of the authors were employees of ONGC during the execution of this work. Mahesh Chandra is the former general manager of ONGC. The authors thank Rebecca Latimer for her comments which were very useful in improving the quality of the paper. Singh thanks Robert Wilson and William Harmony of RepsolYPF for reviewing the manuscript and improving its readability.

Corresponding author: vsingh@repsolypf.com; ak_sri3@rediffmail.com